Supplemental Material: Superconductivity of repulsive spinless fermions with sublattice potentials

Yuchi He,[1] Kang Yang,[2] Jonas B. Hauck,[1] Emil J. Bergholtz,[2] and Dante M. Kennes[1,3]

[1] *Institut für Theorie der Statistischen Physik, RWTH Aachen University and JARA—Fundamentals of Future Information Technology, 52056 Aachen, Germany*

[2] *Department of Physics, Stockholm University, AlbaNova University Center, 106 91 Stockholm, Sweden*

[3] *Max Planck Institute for the Structure and Dynamics of Matter, Center for Free Electron Laser Science, 22761 Hamburg, Germany*

(Dated: January 4, 2023)

I. SUPPLEMENTAL MATERIAL

A. Schrieffer-Wolff transformation

The ground state at filling $n = 1$ is given by all A sites occupied. We use the Schrieffer-Wolff transformation to find the low-energy physics when extra electrons are brought in by doping. The Hamiltonian is comprised of a kinetic part H_k which creates high-energy excitation and an interaction part H_U which controls the zero-doping state. The Schrieffer-Wolff transformation is to eliminate the high-energy kinetic Hamiltonian order by order through a unitary transformation $\exp(iS)$

$$H' = e^{iS} H e^{-iS} = H + [iS, H] + \frac{1}{2}[iS, [iS, H]] + \dots . \tag{S1}$$

The transformation operator is expanded in the order of t/V or t/U, $S = S^1 + S^{(2)} + \dots$. For this purpose, we decompose the kinetic Hamiltonian into the terms preserving the interaction $H_{00}^{(0)}$ and those creating higher energy excitations $\tilde{H}_k$. The aim of $S^{(1)}$ is to eliminate those components $\tilde{H}_k$

$$[iS^{(1)}, H_U] = -\tilde{H}_k, \quad H_k = H_{00}^{(0)} + \tilde{H}_k \text{ and } [\tilde{H}_k, H_U] \neq 0, [H_{00}^{(0)}, H_U] = 0 \ . \tag{S2}$$

The SW transformed Hamiltonian to the order of t^2/U is given by the sum $[iS^{(1)}, H_k] + [iS^{(1)}, [iS^{(1)}, H_U]]/2 = [iS^{(1)}, \tilde{H}_k]/2 + [iS^{(1)}, H_{00}^{(0)}]$. The effective theory is obtained by projecting this expression to the state with A occupied.

To obtain $S^{(1)}$, it is more convenient to decompose H_k into different ladder operators of the onsite potential and the nearest-neighbor repulsion. We do this first for the hopping process from an A site to a nearby B site. It increases the onsite potential by D. The nearest-neighbor repulsion brought by this process depends on the number of neighbors of A and B, $\delta E = (n_B - n_A)V$. With these observations, the kinetic Hamiltonian is decomposed as

$$\begin{aligned} H_k &= \left(H_{00}^{(0)} + H_A\right) + \left(\sum_{m,n} H_{m,n}^{+} + H_{m,n}^{-}\right) \\ &= \left(t' \sum_{ij} c_{i,B}^{\dagger} c_{j,B} + t' \sum_{ij} c_{i,A}^{\dagger} c_{j,A}\right) + \left(t \sum_{j,r,m,n} P_{m,j+r}^{B} c_{j+r,B}^{\dagger} c_{j,A} P_{n,j}^{A} + t \sum_{j,r,m,n} P_{m,j-r}^{A} c_{j-r,A}^{\dagger} c_{j,B} P_{n,j}^{B}\right), \end{aligned} \tag{S3}$$

where the next-nearest-neighbor hopping includes terms preserving H_U and those connecting states with different distributions of A particles. The operators $P_{m,j}^{A/B}$ are projection into the state where the particle A/B at unit cell j has m neighbors occupied. They can be written in terms of the sum over the product operators $\prod_r n_r \prod_{r'}(1 - n_{r'})$, where r, r' are the occupied/unoccupied neighbors. Notice that m, n cannot be larger than $N - 1$, where N is the number of nearest neighbors in this lattice, as the hopping operators in the middle of Eq. (S3) always eliminate one neighbor. One can verify the following commutation relations

$$[H_U, H_{m,n}^{\pm}] = [\pm D + (m - n)V] H_{m,n}^{\pm}. \tag{S4}$$

With these relations, we can define the leading order transformation for the AB hopping to be

$$iS^{(1)}_{AB} = \sum_{m,n} \frac{H^+_{m,n}}{D+(m-n)V} - \frac{H^-_{m,n}}{D-(m-n)V}. \tag{S5}$$

Such similar expressions $S^{(1)}_{AA}, S^{(1)}_{BB}$ can also be obtained for the AA, BB hopping with different numbers of neighbors occupied. So $S^{(1)}$ is comprised of operators that create excitations of H_U. The observation is that those $S^{(1)}_{AA}, S^{(1)}_{BB}$ terms annihilate the state with all A sites occupied. So their contribution to the second order expansion $[iS^{(1)}, \tilde{H}_k]/2$ vanishes after the projection. What are left are terms diagonal in H_U. The resulting expression $[iS^{(1)}, H^{(0)}_{00}] \simeq t't/U$ is off-diagonal in the ground state of H_U. It will be further eliminated to the order $1/U^2$ by the second-order SW transformation. So we can neglect it at the order of $1/U$. The Hamiltonian is simplified to a quadratic form of $H^{\pm}_{m,n}$. As the low energy physics is obtained by projecting H' to the state with all A sites occupied, this requires the total excitation should have equal numbers of $+$ and $-$ and the sum of $m-n$ should vanish. As $H^-_{m,n}$ annihilates the low-energy manifold, it ends up with the following equation

$$H'_{\text{eff}} = -\sum_{m',n} \frac{H^-_{m',m'+N-n} H^+_{N,n}}{D+(N-n)V}. \tag{S6}$$

As the occupation on site A must be conserved, there are two situations in the above summation. When the bond operators in $H^-_{m',m'+N-n}$ and $H^+_{N,n}$ are taking the same one, we obtain density interaction terms. When they differ, we have hopping terms for B fermions. It is more convenient to write out the Hamiltonian for the four neighbors around one A site. Choosing (i,j,k,l) to be the four neighbors of a particle A, we have the following terms for the density interaction part

$$H^U_4 = -\frac{4t^2}{D+3V}(1-n_i)(1-n_j)(1-n_k)(1-n_l), \tag{S7}$$

$$H^U_3 = -\frac{3t^2}{D+2V}(1-n_i)(1-n_j)(1-n_k)n_l + \text{PM}, \tag{S8}$$

$$H^U_2 = -\frac{2t^2}{D+V}(1-n_i)(1-n_j)n_k n_l + \text{PM}, \tag{S9}$$

$$H^U_1 = -\frac{t^2}{D}(1-n_i)n_j n_k n_l + \text{PM}, \tag{S10}$$

where PM means *distinct* combinations obtained by permuting i,j,k,l. For the hopping processes from $i \to j$, we need that the A particle has neighbor i occupied before the hopping and j occupied after the hopping. These terms are given by

$$H^k_3 = \frac{t^2}{D+2V} c^\dagger_{i,B} c_{j,B}(1-n_k)(1-n_l) + \text{PM}, \tag{S11}$$

$$H^k_2 = \frac{t^2}{D+V} c^\dagger_{i,B} c_{j,B} n_k (1-n_l) + \text{PM}, \tag{S12}$$

$$H^k_1 = \frac{t^2}{D} c^\dagger_{i,B} c_{j,B} n_k n_l + \text{PM}. \tag{S13}$$

Similarly, PM means *distinct* combinations obtained by permuting i,j,k,l

Now we collect the contributions together. We have two-body, three-body and four-body interactions:

$$H'_{U,\text{eff}} = \sum_{ij} U_2 n_i n_j + \sum_{ijk} U_3 n_i n_j n_k + \sum_{ijkl} U_4 n_i n_j n_k n_l. \tag{S14}$$

The summation of i,j,k,l is defined by counting the different two-, three- and four-combinations of the neighbors around every A site. So the two-body interaction along the diagonal of the square lattice should be counted twice. Their coefficients are given by

$$U_2 = -\frac{2t^2}{D+V} + \frac{6t^2}{D+2V} - \frac{4t^2}{D+3V}, \tag{S15}$$

$$U_3 = -\frac{t^2}{D} + \frac{6t^2}{D+V} - \frac{9t^2}{D+2V} + \frac{4t^2}{D+3V}, \tag{S16}$$

$$U_4 = \frac{4t^2}{D} - \frac{12t^2}{D+V} + \frac{12t^2}{D+2V} - \frac{4t^2}{D+3V}. \tag{S17}$$

The effective hopping Hamiltonian can be assisted by the other two neighbors around each A site

$$H'_{k,\text{eff}} = \sum_{ij} \lambda_0 c^\dagger_{i,B} c_{j,B} + \sum_{ijk} \lambda_1 c^\dagger_{i,B} c_{j,B} n_k + \sum_{ijkl} \lambda_2 c^\dagger_{i,B} c_{j,B} n_k n_l, \tag{S18}$$

where the hopping parameters are

$$\lambda_0 = \frac{t^2}{D+2V} \tag{S19}$$

$$\lambda_1 = \frac{t^2}{D+V} - \frac{t^2}{D+2V} \tag{S20}$$

$$\lambda_2 = \frac{t^2}{D} - \frac{2t^2}{D+V} + \frac{t^2}{D+2V}. \tag{S21}$$

All the parameters as a function of V/D are plotted in Fig. S1.

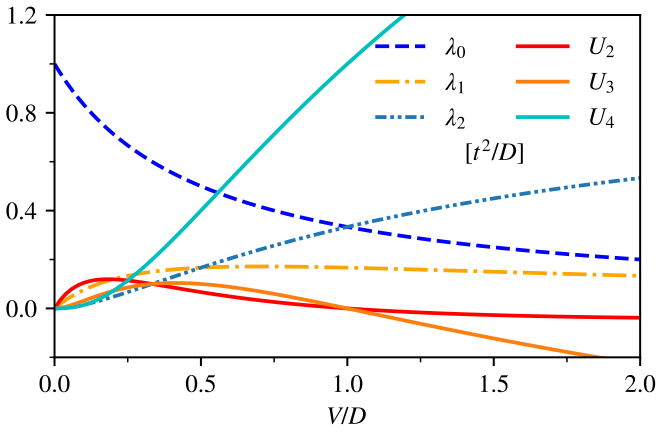

FIG. S1. Parameters of the large-D effective theory of the square lattice model.

B. Continuum theory for low doping

The effective inverse mass tensor at the two valleys are

$$m_\pm^{-1} = a^2 \begin{pmatrix} 4t'_B \mp 2t_B & 0 \\ 0 & 4t'_B \pm 2t_B, \end{pmatrix} \tag{S22}$$

where the subscript $+$ $(-)$ denotes the valley located at $(0,\pi)$ $((\pi,0))$. Recall that the two valleys being minimum is given by the condition $|t'_B/t_B| > 0.5$. We see that the mass tensor is diagonal in the coordinate we choose, and there is mass anisotropy for each valley.

We introduce the center-of-mass coordinates: $\delta\mathbf{r} = \mathbf{r}_+ - \mathbf{r}_-, \mathbf{R} = \bar{m}_+\mathbf{r}_+ + \bar{m}_-\mathbf{r}_-$, where $\bar{m}_\pm = m_\pm/\operatorname{Tr}(m_\pm)$. The (first-quantized) kinetic Hamiltonian of the two particles can be written as $(\nabla^T_{\delta\mathbf{r}}\mu^{-1}\nabla_{\delta\mathbf{r}} + \nabla^T_{\mathbf{R}}M^{-1}\nabla_{\mathbf{R}})/2$. We find that the relative inverse mass tensor μ^{-1} is isotropic: $\mu^{-1} = \mu_0^{-1}I$, where $\mu_0^{-1} = (8a^2t'_B)$ and I is the 2×2 identity matrix. The continuum approximation of the two-particle problem is similar to that of the honeycomb model [1]. The two-particle binding energies can be calculated in the center-of-mass reference frame [1]:

$$E_{\text{bp}} = e_{\text{bp}}[e^{2\pi/(\mu_0|g|)} - 1]/\mu_0, \tag{S23}$$

where $\mu_0 = (8a^2t'_B)^{-1}$ is the relative mass. The result is independent of the specific value of t_B (t' in the full model) as long as the ground states of single fermion [two fermions] are in the $(0,\pi)$ or $(\pi,0)$ $[(\pi,\pi)]$ momentum sector, consistent with the microscopic Hamiltonian being independent of t_B in the two-particle (π,π) sector. We fit e_{bp} using exact data in the small V/D region and plot the continuum effective result together with the exact result in Fig. S2. Different from the honeycomb model, the binding energies will drop for large V because $|g|$ will decay to zero for large V instead of converging to a constant.

To extract coefficients of interaction in the continuum theory, we write the correlated hopping as

$$\begin{aligned}\lambda_1 \sum_{i,j,k} c^\dagger_i c^\dagger_j c_j c_k =& \lambda_1 \sum_{\substack{i,j,k,\\ \mathbf{k},\mathbf{k}',\mathbf{q},\sigma_i}} \psi^\dagger_{\sigma_1,\mathbf{k}-\mathbf{q}} \psi^\dagger_{\sigma_2,\mathbf{k}'+\mathbf{q}} \psi_{\sigma_3,\mathbf{k}'} \psi_{\sigma_4,\mathbf{k}} \\ &\times e^{-i(\mathbf{K}_{\sigma_1}+\mathbf{k}-\mathbf{q})\cdot\mathbf{a}_i - i(\mathbf{K}_{\sigma_2}-\mathbf{K}_{\sigma_3}+\mathbf{q})\cdot\mathbf{a}_j} \\ &\times e^{i(\mathbf{K}_{\sigma_4}+\mathbf{k})\cdot\mathbf{a}_k},\end{aligned} \tag{S24}$$

where $\mathbf{a}_i$ is taken from the four vectors connecting A to its nearest B neighbours. The variables $\mathbf{k},\mathbf{q},\mathbf{k}'$ are taken to be much smaller than $|\mathbf{K}^+ - \mathbf{K}^-|$. Similarly, the repulsion term is rewritten as

$$\begin{aligned}U_2 \sum_{ij} c^\dagger_i c^\dagger_j c_j c_i =& U_2 \sum_{\substack{i,j,\mathbf{q},\\ \mathbf{k},\mathbf{k}',\sigma_i}} \psi^\dagger_{\sigma_1,\mathbf{k}-\mathbf{q}} \psi^\dagger_{\sigma_2,\mathbf{k}'+\mathbf{q}} \psi_{\sigma_3,\mathbf{k}'} \psi_{\sigma_4,\mathbf{k}} \\ &\times e^{-i(\mathbf{K}_{\sigma_1}-\mathbf{K}_{\sigma_4}-\mathbf{q})\cdot\mathbf{a}_i - i(\mathbf{K}_{\sigma_2}-\mathbf{K}_{\sigma_3}+\mathbf{q})\cdot\mathbf{a}_j}.\end{aligned} \tag{S25}$$

The continuum interactions between different valleys and inside the same valley are given by taking appropriate combinations of σ_i and their anti-symmetrized partners.

The result of inter-valley interaction has been given in the main text. Now we consider intra-valley interaction with finite doping. We consider the weak interacting

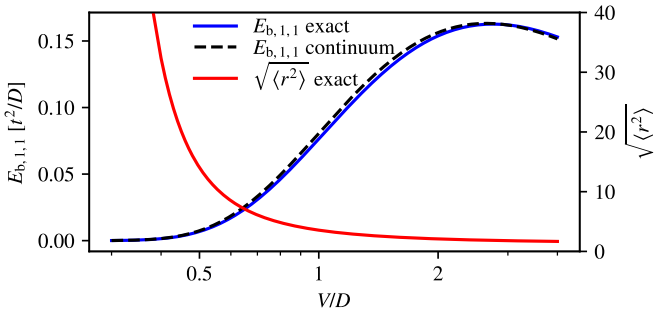

FIG. S2. Binding energies and bound states sizes of two fermions for the effective square lattice model with two valleys. The dashed line denotes the continuum effective theory with one fitting parameter given by matching small V/D data.

limit and discuss the interaction between modes on the Fermi surface of a valley, for example, the + valley. Here the momenta are defined as the deviation to $(0, \pi)$. In general, we have.

$$\sum_{\mathbf{k},\mathbf{k}',\mathbf{q}} g(\mathbf{k},\mathbf{k}',\mathbf{q})\psi^\dagger_{+,\mathbf{k}-\mathbf{q}}\psi^\dagger_{+,\mathbf{k}'+\mathbf{q}}\psi_{+,\mathbf{k}'}\psi_{+,\mathbf{k}} \tag{S26}$$

We focus on two-particle scattering with net zero deviation to $\mathbf{K}_+$ and small doping (momenta is small enough to perform Taylor expansion).

$$\sum_{\mathbf{q}_1,\mathbf{q}_2} \tilde{g}(\mathbf{q}_1,\mathbf{q}_2)\psi^\dagger_{+,\mathbf{q}_1}\psi^\dagger_{+,-\mathbf{q}_1}\psi_{+,-\mathbf{q}_2}\psi_{+,\mathbf{q}_2} \tag{S27}$$

Set $\mathbf{q}_1 = \mathbf{q}_2$ and $\mathbf{q}_1 = -\mathbf{q}_2$ respectively, we can obtain the density-density interaction, $\propto [2\lambda_1(q_{1,x}^2 - q_{1,y}^2) + U_2(q_{1,x}^2 + q_{1,y}^2)]n_+(\mathbf{q}_1)n_+(-\mathbf{q}_1)$. With the Fermi surface shape close to an eclipse with the long axis along the y direction, and $\lambda_1 \approx U_2$ for $V/D < 1$ (Fig. S1), such interaction in most momenta is attractive.

C. Few-particle-doping binding energy with finite D/t

Here, we discuss few-particle-doping binding energies of the full model with finite $D/t = 10, 5$. The binding energies, in the unit of t^2/D, are in general smaller for smaller D/t . However, even for $D/t = 5$, we find no substantial difference for inferred stable pairing region, compared to the effective model with $D/t = \infty$.

As an alternate of binding energy per particle, we represent the results as binding energies for forming bound states with composites. For two-particle and three-particle bound states, the existence of bound states can be seen from a positive $E_{\mathrm{b},1,1} = 2E_1 - E_0 - E_2$ and $E_{\mathrm{b},1,2} = E_1 + E_2 - E_0 - E_3$ respectively. These quantities are plotted in Fig. S3. Binding energy per particle can be deduced from them. The existence of three-particle bound states does not mean that three-particle bound states are more favored than pairs for dilute doping. Favored bound states have the largest binding energy per particle.

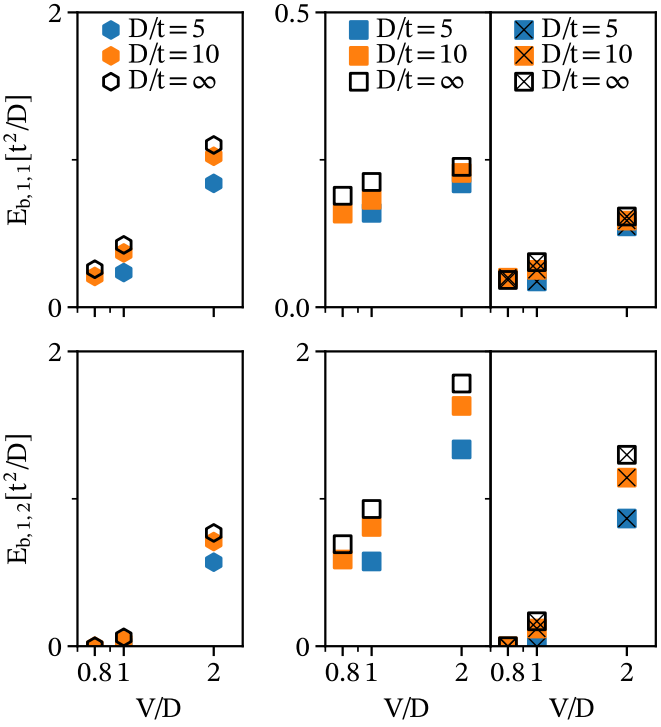

FIG. S3. Binding energies. The binding energies of two fermions are shown in the first row from left to right for the honeycomb lattice model and the square lattice model without t' term and for $t' = \lambda_0$. Correspondingly, the binding energies for a fermion pair and a fermion to form a three-fermion bound state are shown in the second row. The plot scale of the $E_{b,1,1}$ of square lattice models is smaller than others'.

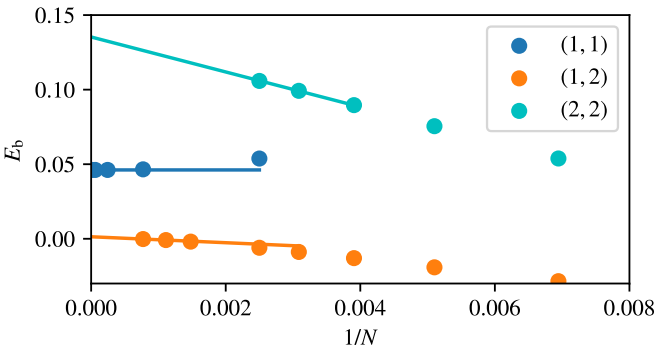

FIG. S4. Binding energy extrapolation. We show an example of extrapolation to obtain Fig. 3 in the main text and Fig. S3 The data are taken from ED for $V/D = 0.8$, $t' = \lambda_0$ of the square lattice.

Some details of the numerical implementation are as follows. For the full (effective) lattice models, we obtain the ground-state energies E_n of finite systems using DMRG (exact) diagonalization. To accurately com-

pute binding energies, we need system sizes larger than the sizes of the bound states. We estimate the finite-size errors by doing $1/N$ extrapolation for data of the two largest systems we obtain. The extrapolated data in Fig. S3 have errors smaller than the size of markers. The periodic boundary condition is implemented in the exact diagonalization, which enables reading the momentum quantum numbers. DMRG is less efficient to deal with periodic conditions along two directions and we thus only implement a periodic boundary condition in one direction while implementing an open boundary condition on the other. In this case, to correctly calculate the bulk binding energy, we find it essential to eliminate the low-energy edge modes. Such modes can be understood by considering the potential and interaction part of the Hamiltonian Eq.(1):$\sum_{\langle i,j\rangle} V n_i n_j + \sum_{i\in B} D n_i$. As A sublattice is almost fully-filled, if a fermion on B sublattice is located at the open boundary rather than in the bulk, it feels less repulsion from the fermions on B sublattice. Consequently, these configurations have lower energy. We find that introducing additional potential terms Vn_i on the boundary of B sublattice can eliminate low-energy edge modes.

D. Weak-coupling results

In the weak coupling regime, we apply a truncated unity functional renormalization group approach. The FRG flavor we employ is a method to construct unbiased single and two-particle interactions from a set of flow equations. While three- and four-body interactions are not counted as objects themselves, they are partially included via virtual processes in the two-particle interaction. We use a sharp energy cutoff [2], thus the critical energy scale can be interpreted as a critical temperature modulo an unknown scaling factor. We calculate the vertex on a 24×24 momentum mesh for both lattices, with a refinement for the bubble integration mesh of 45×45. On the square lattice, we include the 25/29 nearest neighbors in the truncated unity per site within the unit cell for the honeycomb/square lattice. We use a Bogacki–Shampine adaptive integrator for the integration of the flow equations, allowing for a maximal absolute error of 10^{-2} per integration step. The results of the FRG simulations are visualized in Fig. S5. To distinguish different phases, we inspect the behavior of the maximal eigenvalues of each channel during the flow in combination with an inspection of the dominant eigenvectors at the end of the flow. These eigenvectors encode symmetries and specific types of instability. In the case of p_y/p_x we find the two eigenvectors to be exactly degenerate. In the real space representation we define $p_{x/y} = \mathrm{sign}(\vec{v}_{x/y}\cdot\vec{d})\delta_{\vec{v}_{x/y},\vec{d}}$ with $\vec{v}_x = (1,0)$, $\vec{v}_y = (0,1)$ and $\vec{d}$ is the vectorial distance between two sites. To distinguish all possible linear combinations $\cos(\theta)p_x + e^{i\phi}\sin(\theta)p_y$ we perform a single-step mean-field calculation and compare the free energy of each starting configuration, as can be seen in Fig. S6. To calculate the Chern number in the gapped phase, we employ the method described in Ref. [3].

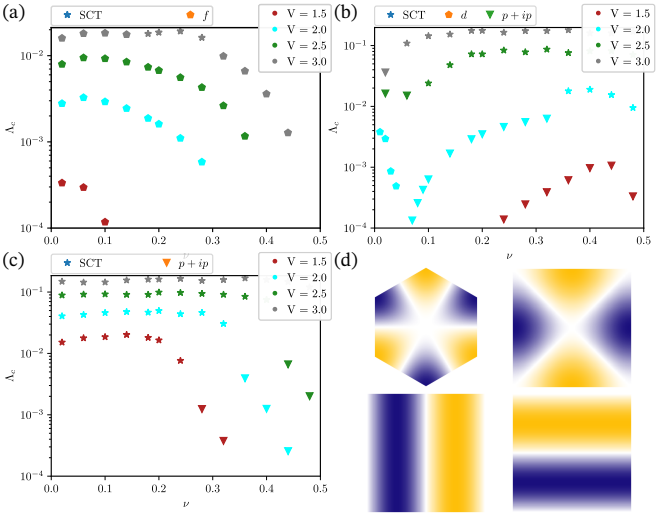

FIG. S5. Results of the FRG simulations for the three different setups and visualization of the f-wave superconductivity. We abbreviate a flow to strong coupling without divergent susceptibility as SCT, and a divergence of the f-wave component of the pairing susceptibility as f-SC. The y-axis displays the critical energy scale, which is linearly dependent on the critical temperature. The x-axis displays the doping. (a) shows the results for a square lattice with $t' = \lambda_0$ and (b) the square lattice with $t' = 0$ results. (c) shows the results for the honeycomb lattice. In all simulations, we kept $D = 10$ and varied V in the given range. (d) visualizes the different superconducting order parameter symmetries encountered, as visualized by the eigenvector of the effective two-particle interaction at the orbital at the Fermi level. The upper left shows an f-wave on the honeycomb lattice, the upper right shows a $d_{x^2-y^2}$-wave on the square lattice. The lower two plots correspond to the degenerate pair p_x and p_y with weak admixture of other dependencies.

E. Details of infinite DMRG calculations

We obtain approximate ground states of the Hamiltonian Eq.(1) defined on infinite cylinders. We do this by optimizing infinite matrix product states via two-site iDMRG algorithm [4]. We implement the conservation of particle numbers, thus the phase diagram Fig. **??** is constructed in terms of doping densities ν. The accuracy of infinite matrix product states can be improved by increasing its bond dimensions (χ, size of the matrices); With efficient optimization, to reach a given accuracy, the required computational resource (e.g. χ) is exponentially large in cylinder circumference. Infinite matrix product states are constructed to be exactly translationally invariant by M lattice unit vector along the axial direction. To implement exact particle number conservation for doping density $\nu = p/q$ (irreducible fraction), M must

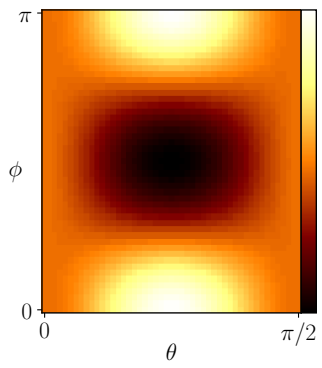

FIG. S6. Free energy minimization in the square lattice with $t' = \lambda_0$, using $\cos(\theta)p_x + e^{i\phi}\sin(\theta)p_y$ as starting values. The combination with the smallest free energy is $\frac{1}{2}(p_x + ip_y)$

be integer multiples of q/L_y. (L_y is the number of lattice unit vectors around the cylinder.) To be compatible with the possible spontaneous breaking of translational symmetry (e.g., charge-density-wave state), M has to be compatible with the enlarged unit cell. As mentioned in the main text, we estimate of correlation lengths of single-particle and pair to infer superconductivity. See Ref. [5, 6] for the definition and extraction methods for one-dimensional correlation lengths. Here, we define the correlation length from the correlation along the axial (infinite) direction. We denote them estimated using bond dimension χ as $\xi_1(\chi)$ and $\xi_2(\chi)$ respectively; the larger the bond dimension, the more accurate the estimation.

[1] V. Crépel and L. Fu, New mechanism and exact theory of superconductivity from strong repulsive interaction, Science Advances **7**, eabh2233 (2021).

[2] W. Metzner, M. Salmhofer, C. Honerkamp, V. Meden, and K. Schönhammer, Functional renormalization group approach to correlated fermion systems, Rev. Mod. Phys. **84**, 299 (2012).

[3] T. Fukui, Y. Hatsugai, and H. Suzuki, Chern numbers in discretized brillouin zone: Efficient method of computing (spin) hall conductances, Journal of the Physical Society of Japan **74**, 1674 (2005).

[4] I. P. McCulloch, Infinite size density matrix renormalization group, revisited, arXiv preprint arXiv:0804.2509 (2008).

[5] Y. He, D. Pekker, and R. S. K. Mong, One-dimensional repulsive hubbard model with mass imbalance: Orders and filling anomaly, Phys. Rev. B **104**, 195126 (2021).

[6] V. Zauner, D. Draxler, L. Vanderstraeten, M. Degroote, J. Haegeman, M. M. Rams, V. Stojevic, N. Schuch, and F. Verstraete, Transfer matrices and excitations with matrix product states, New Journal of Physics **17**, 053002 (2015).